Intermediate mass fragment emission as a probe of nuclear dynamics

D. R. Bowman, C. M. Mader, G. F. Peaslee, W. Bauer, N. Carlin,* R. T. de Souza,†
C. K. Gelbke, W. G. Gong,‡ Y. D. Kim,§ M. A. Lisa, W. G. Lynch, L. Phair, M. B. Tsang, and C. Williams
National Superconducting Cyclotron Laboratory and Department of Physics and Astronomy, Michigan State University, East Lansing, Michigan 48824

N. Colonna, K. Hanold, M. A. McMahan, G. J. Wozniak, and L. G. Moretto
Nuclear Science Division and Accelerator and Fusion Research Division, Lawrence Berkeley Laboratory, Berkeley, California 94720

W. A. Friedman
Department of Physics, University of Wisconsin, Madison, Wisconsin 53706
(Received 15 June 1992)

Element distributions and fragment multiplicity distributions have been measured for $E/A=50$ MeV $^{129}Xe+^{12}C$, ^{27}Al, ^{51}V, ^{nat}Cu, ^{89}Y, and ^{197}Au reactions using a low threshold 4π detector. Both distributions show a strong correlation with the detected charged particle multiplicity and a large degree of target independence. The measured distributions are compared with hybrid model calculations which incorporate important dynamical aspects in both the preequilibrium and statistical emission phases. Results of these calculations are in reasonable agreement with the data. However, uncertainties with regard to the compressibility of nuclear matter remain due to uncertainties in the coupling of the two models.

PACS number(s): 25.70.Pq

I. INTRODUCTION

Multifragment disintegrations of highly excited nuclear systems have recently been studied using a new generation of electronic detectors [1–8]. A number of theoretical investigations indicate that this process may become a dominant decay mode of nuclear systems at moderate temperature ($T\approx 10$ MeV). These models predict fragment formation to occur as a result of volume instabilities at reduced nuclear density ($\rho\approx 0.5\rho_0$) [9–19] or surface instabilities of the Rayleigh-Taylor variety [20,21]. The former models include those based upon the assumption that nuclear systems undergo a rapid disassembly in the region of spinodal instability in the liquid-gas phase diagram of nuclear matter [9–16]. Multifragment decay probabilities for rapid breakup at low density also have been calculated by using canonical or microcanonical statistical approximations [17–19]. As an alternative to these completely static equilibrium calculations, another class of statistical models take a rate equation approach in calculating fragment emission [22–29]. The rate equation model of Ref. [29] also incorporates a schematic description of expansion dynamics wherein a hot source can undergo isotropic expansion while emitting light particles and intermediate mass fragments (IMF's). We refer to this model as the expanding-emitting-source model (EES).

Statistical models stipulate the attainment of an equilibrated system as an initial condition, without addressing the question whether such an assumption is consistent with the dynamical evolution of the early stage of the reaction. A number of inclusive investigations have shown that a significant portion of the emitted fragments must be attributed to processes in which complete equilibrium of the composite system has not been attained [30–34]. Hence the neglect of nonequilibrium emission in the early stages of the reaction by the present statistical approaches may be unjustified.

Molecular-dynamics transport models [35,36] have been developed specifically to describe the nonequilibrium aspects of nuclear collisions. However, recent comparisons with data indicate that the fragment multiplicities calculated with these models are much smaller than those observed experimentally [5,6,37]. This failure of the molecular-dynamics models is not presently understood and is currently the subject of intense theoretical research. Despite their neglect of nonequilibrium dynamics, statistical calculations of the decay of expanding compound nuclei have been much more successful than the molecular-dynamics models in reproducing the ratio of light charged particles to IMF's [5,6] and the observed charge distributions [8,37].

The IMF multiplicities predicted by the EES model are sensitive to the minimum density attained by the decaying systems [5,6]. Smaller densities lead to enhanced

*Present address: Instituto de Fisica, Universidade de Sao Paulo, C. Postal 20516, CEP 01498, Sao Paulo, Brazil.
†Present address: IUCF and Department of Chemistry, Indiana University, Bloomington, IN 47405.
‡Present address: Lawrence Berkeley Laboratory, Berkeley, CA 94720.
§Present address: Indiana University Cyclotron Facility, Bloomington, IN 47405.

IMF emission rates. The minimum density attained in the model depends upon the initial radial kinetic energy when the system begins to expand from $\rho=\rho_0$, as well as on the nuclear compressibility [6] and the thermal pressure. This initial radial kinetic energy of the composite system is strongly influenced by the compression-decompression dynamics in the initial stages of the reaction, which, in turn, should depend upon the mass ratio of the projectile and target. For asymmetric systems such as ^{129}Xe+^{27}Al, compressional effects and radial expansion velocities should be small; for more symmetric systems such as ^{129}Xe+^{197}Au, an initial compression phase may be followed by a rapid expansion phase.

In order to investigate such mass-dependent effects, we have measured multifragment production in ^{129}Xe-induced reactions on ^{12}C, ^{27}Al, ^{51}V, ^{nat}Cu, ^{89}Y, and ^{197}Au targets at $E/A=50$ MeV. By studying different projectile-target combinations at fixed relative velocity, one may hope to explore how fragment formation is influenced by differing amounts of compression and subsequent expansion. To compare with theoretical predictions, we have chosen to focus on central collisions. By these means, we expect to select events with a maximum degree of equilibration [38], for which comparisons with statistical models of fragment emission should be most appropriate, and to reduce uncertainties associated with the effects of angular momentum.

Measured fragment multiplicities have been previously compared with predictions of the EES model [5,6]. In these works a range of values for the initial thermal energy, kinetic energy of radial expansion, and source size were selected. The extent to which these selected values are compatible with our best understanding of the early nonequilibrium stages of these reactions is not clear. We now attempt to obtain specific input parameters for the EES model from solutions of the Boltzmann-Uehling-Uhlenbeck (BUU) transport equation [39]. Such a hybrid calculation permits the treatment of compression and energy deposition by the BUU equation in the initial phase of the reaction and the treatment of fragment formation by the EES model in the expansion phase.

Previous hybrid calculations [40–42] have involved sharp discontinuities between the dynamical preequilibrium stage and the completely static equilibrium decay stage. Dynamical models typically indicate that decaying systems undergo a rapid expansion, and aspects of this expansion dynamics should also be considered in the later stages of the reaction. By coupling a transport model (BUU) with a statistical decay model which also incorporates dynamics (EES), essential features of the expansion dynamics from the preequilibrium phase can be retained.

We will compare our experimental results with a hybrid calculation which employs independent models best suited to different phases of the reaction. In this comparison we assess the sensitivity of the final results to the uncertainties inherent in the matching of the models. Since compressibility in both the initial and final stages of the reaction is assumed to influence the production of IMF's, we attempt to evaluate the extent to which the current data can be used to constrain this important theoretical parameter.

This paper is organized as follows: The experimental details are given in Sec. II; the experimental results are presented in Sec. III; in Sec. IV, the models are presented, the coupling of the models is discussed, and comparisons with the data are shown; a summary of the results is given in Sec. V.

II. EXPERIMENTAL DETAILS

The experiment was performed using the K1200 Cyclotron of the National Superconducting Cyclotron Laboratory at Michigan State University. A ^{129}Xe beam of energy $E/A=49.8$ MeV and intensity $\sim 10^7$ particles/s impinged upon targets of ^{12}C, ^{27}Al, ^{51}V, ^{nat}Cu, ^{89}Y, and ^{197}Au, with thicknesses of 1.1, 2.0, 1.9, 2.3, 1.0, and 1.0 mg/cm^2, respectively. The beam was delivered to the 92 in. scattering chamber with a typical beam spot diameter of 2–3 mm.

Light charged particles and fragments of $Z=1$–20 emitted at laboratory angles of 16°–160° were detected using the MSU Miniball [43]. As configured for this experiment, the Miniball consisted of 171 fast plastic (40 μm)–CsI(2 cm) phoswich detectors, with a solid angle coverage of approximately 87% of 4π. Identification thresholds for $Z=3$, 10, and 18 fragments were $\sim$2, 3, and 4 MeV/nucleon, respectively. Less energetic charged particles with energies of >1 MeV/nucleon were detected in the fast plastic scintillator foils, but not identified by Z value. Isotopic identification was achieved for hydrogen and helium isotopes with energies <75 MeV/nucleon. Energy calibrations were performed using elastically scattered ^{12}C beams at forward angles and by using the hydrogen punchthrough points of the more backward detectors to normalize to existing calibration data [44]. The energy calibrations are estimated to be accurate to about 5% at angles $<31°$ and to about 10% for the more backward angles.

At very forward angles 2°–16°, fragments of charge $Z=1$–54 were detected with high resolution using a 16-element Si(300 μm)–Si(Li)(5 mm)–plastic(7.6 cm) array [45] with a geometrical efficiency of $\sim$64%. Where counting statistics allowed, individual atomic numbers were resolved for $Z=1$–54. Representative detection thresholds for fragments of $Z=2$, 8, 20, and 54 fragments were approximately 6, 13, 21, and 27 MeV/nucleon. Energy calibrations were obtained by directing 18 different beams ranging from $Z=1$ to 54 into each of the 16 detector elements [46]. The energy calibration of each of these detectors is accurate to better than 1%, and position resolutions of ± 1.5 mm are obtained.

The complete detector system subtended angles from 2° to 160° with respect to the beam axis and had a geometric acceptance of >88% of 4π. As a precaution against secondary electrons, detectors at angles $>100°$ were covered with Pb-Sn foils of thickness 5.05 mg/cm^2 (this somewhat increased the detection thresholds for these detectors). Both the Miniball and the forward array were cooled and temperature stabilized. Gain drifts of the Miniball photomultiplier tubes were monitored with a light pulser system, and corrections were applied off-line.

Data were taken under two trigger conditions: At least two Miniball elements triggered or at least one intermediate mass fragment (IMF: $Z \geq 3$) was observed in the forward array. Further details about the electronics and data-acquisition systems are given in Ref. [43]. Because of the low beam intensity, random coincidences between detectors were negligible.

III. EXPERIMENTAL RESULTS

Probability distributions of the measured total charged particle multiplicity N_c are shown in Fig. 1 for the $E/A = 50$ MeV ^{129}Xe+^{12}C, ^{27}Al, ^{51}V, ^{nat}Cu, ^{89}Y, and ^{197}Au systems. Each of the distributions shows a similar qualitative trend: a peak at very small values of N_c, followed by a broad flat region at intermediate multiplicity, and finally a smooth falloff at the largest values of N_c. The multiplicity distributions extend to progressively larger values as the target mass, and hence total center-of-mass (c.m.) energy, increases. Assuming that total multiplicity scales monotonically with impact parameter, we include at the top of each panel a rough estimate of the impact parameter scale b/b_{max} using the geometric prescription of Ref. [47]:

$$\frac{b(N_c)}{b_{max}} \approx \left[\int_{n_c=N_c}^{n_c=\infty} \frac{dP(n_c)}{dn_c} dn_c \right]^{1/2}, \quad (1)$$

where b_{max} is the impact parameter corresponding to the most peripheral collisions detected.

The two-dimensional relationships between N_c and the intermediate mass fragment multiplicity N_{IMF} are shown in Fig. 2. For each projectile-target combination, the average fragment multiplicity increases with increasing charged particle multiplicity. Larger fragment multiplicities are observed for the heavier targets, for which a larger c.m. energy is available and for which the charged particle multiplicity distributions extend to greater values.

Figure 3 shows IMF multiplicity distributions gated on different values of N_c. As reported previously [5], the average fragment multiplicity for the most violent ^{129}Xe+^{197}Au collisions reaches a value >6. This is the largest average fragment multiplicity yet observed in a nuclear reaction. Such large IMF multiplicities have not been observed even at very high bombarding energies of several hundred MeV per nucleon [1,4].

We can investigate the relationship between the total charged particle multiplicity and the intermediate mass fragment multiplicity more quantitatively by evaluating the mean values $\langle N_{IMF} \rangle$ and the variances σ^2_{IMF} of the intermediate mass fragment multiplicity distributions as a function of charged particle multiplicity. The relationships between $\langle N_{IMF} \rangle$ and N_c for the six systems are shown in Fig. 4. Over a broad range of charged particle multiplicity, the relation between $\langle N_{IMF} \rangle$ and N_c is nearly independent of the system. Correlations between the fragment multiplicity and other experimental observables which have been related to the impact parameter have also been shown to be insensitive to the target nucleus in heavy-ion reactions at both intermediate [3] and high

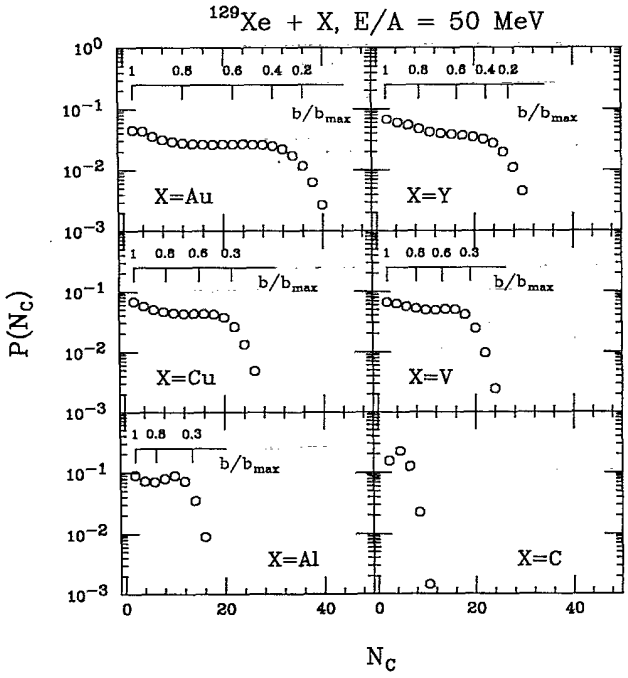

FIG. 1. Probability distributions of charged particle multiplicity, $P(N_c)$, measured for the $E/A = 50$ MeV ^{129}Xe+^{197}Au, ^{89}Y, ^{nat}Cu, ^{51}V, ^{27}Al, and ^{12}C reactions. The panels are labeled by target. For orientation, rough estimates of the impact parameter scales calculated using Eq. (1) [47] are shown.

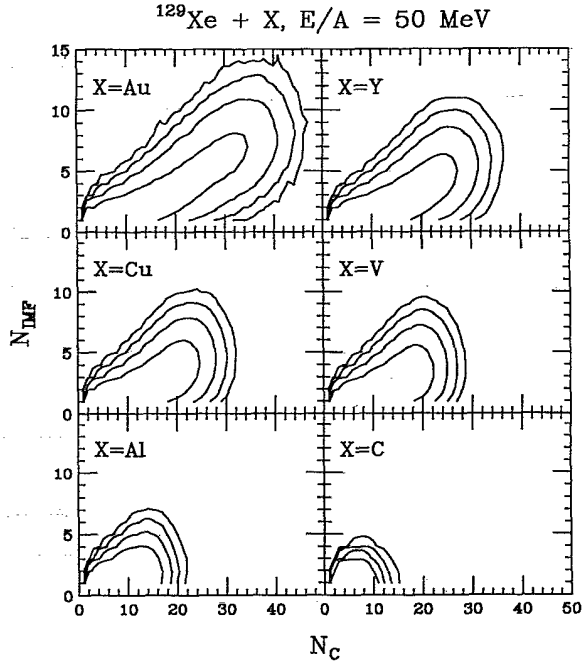

FIG. 2. Logarithmic contour plots showing the measured relationship between total charged particle multiplicity and IMF multiplicity for $E/A = 50$ MeV ^{129}Xe+^{197}Au, ^{89}Y, ^{nat}Cu, ^{51}V, ^{27}Al, and ^{12}C reactions. The panels are labeled by target. Each succeeding contour corresponds to a factor of 6 increase in yield.

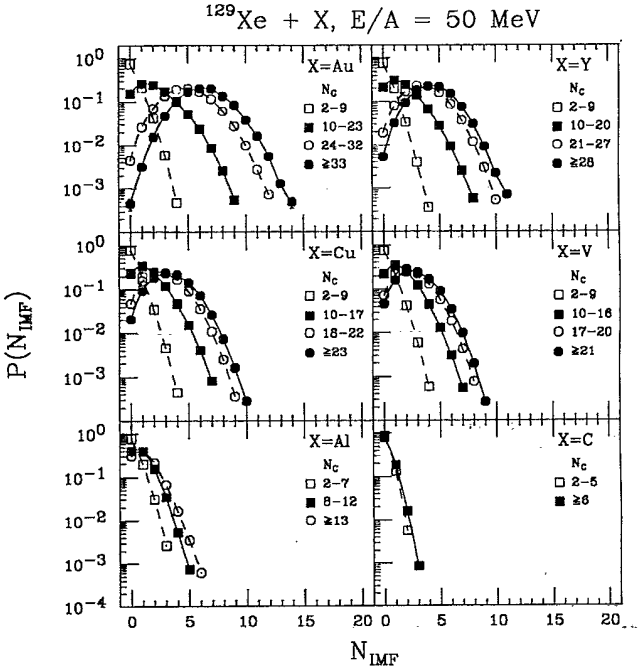

FIG. 3. Probability distributions of intermediate mass fragment multiplicity, $P(N_{IMF})$, measured for the $E/A=50$ MeV ^{129}Xe+^{197}Au, ^{89}Y, ^{nat}Cu, ^{51}V, ^{27}Al, and ^{12}C reactions for several gates on total charged particle multiplicity N_c. The panels are labeled by target. The different symbols represent the indicated multiplicity gates. The solid and dashed lines guide the eye through the data points.

bombarding energy [7]. Deviations from the global dependence of $\langle N_{IMF}\rangle$ on N_c are found only in the tails of the charged particle multiplicity distributions. In general, the charged particle multiplicity should be strongly correlated with energy deposition, and a unique dependence on N_c indicates a unique sensitivity to energy deposition. In the tails of the N_c distributions, deviations must be expected, since here variations in N_c represent fluctuations in the charged particle multiplicity and not changes in energy deposition.

The variances of the fragment multiplicity distributions as a function of total charged particle multiplicity are plotted in the top panel of Fig. 5. The variances become larger as the total charged particle multiplicity increases. Once again, a large degree of target independence is observed. In the bottom panel of Fig. 5, the ratios of the variances to the centroids are plotted. These ratios are nearly equal to 1 for small values of N_c and decrease with increasing charged particle multiplicity. Since the ratios are less than 1, the distributions are narrower than Poisson distributions.

Figure 6 shows charge distributions gated on different values of N_c. For gates on small values of N_c, the charge distributions are very steep, and large yields of projectile-like fragments with $Z>40$ are observed in the Si array at forward angles. With increasing charged particle multiplicity, the charge distributions become progressively less steep, and the heavy-fragment peak shifts to smaller Z and becomes smaller in magnitude. Virtually no fragments of $Z>25$ are observed for charged particle multiplicities $N_c \geq 25$, and the charge distributions become independent of the total charged particle multiplicity for $N_c>20$.

In order to compare the decay properties of the six systems quantitatively, we have fitted the charge distributions over the range of $3 \leq Z \leq 10$ with an exponential function $Y(Z)=Ae^{-\alpha Z}$. The extracted parameters α, shown as a function of N_c in Fig. 7, are nearly independent of target mass. The fitting parameters depend mainly on the measured charged particle multiplicity. As with

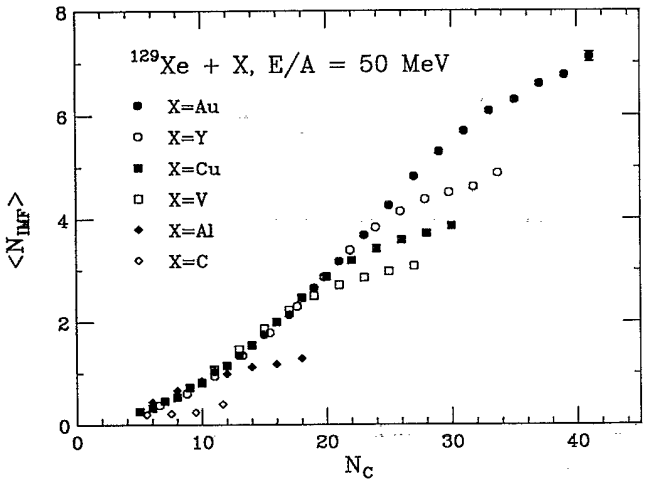

FIG. 4. Average IMF multiplicity $\langle N_{IMF}\rangle$ measured for a given total charged particle multiplicity N_c for $E/A=50$ MeV ^{129}Xe+^{197}Au, ^{89}Y, ^{nat}Cu, ^{51}V, ^{27}Al, and ^{12}C reactions. The different symbols represent the indicated targets.

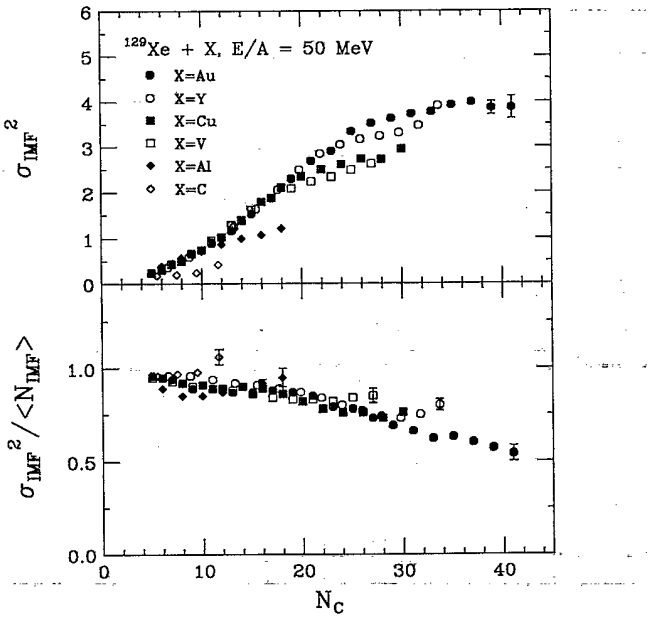

FIG. 5. Second moments of the IMF multiplicity distributions (top panel) and the ratio of the second to first moments of the IMF multiplicity distributions (bottom panel) for $E/A=50$ MeV ^{129}Xe+^{197}Au, ^{89}Y, ^{nat}Cu, ^{51}V, ^{27}Al, and ^{12}C reactions. The different symbols represent the indicated targets.

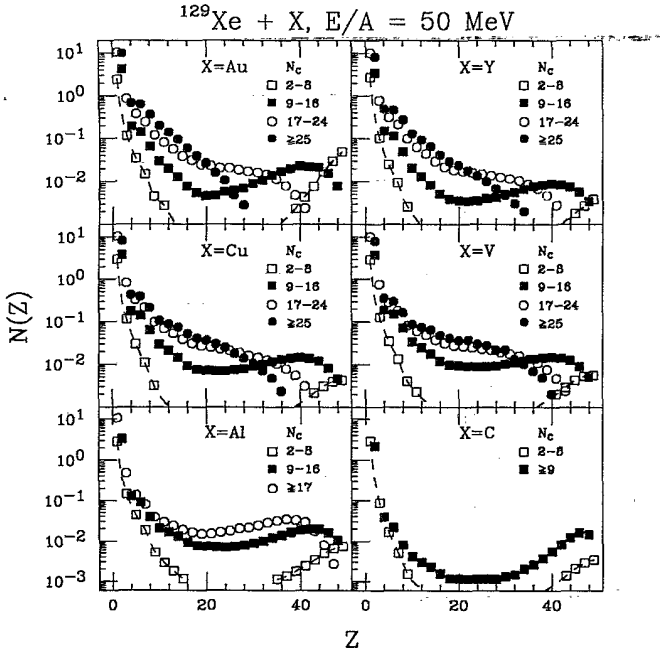

FIG. 6. Charge distributions measured for the $E/A=50$ MeV ^{129}Xe+^{197}Au, ^{89}Y, ^{nat}Cu, ^{51}V, ^{27}Al, and ^{12}C reactions for several gates on total charged particle multiplicity N_c. The panels are labeled by target. The different symbols represent the indicated multiplicity gates. The solid and dashed lines guide the eye through the data points.

the $\langle N_{\rm IMF}\rangle$ to N_c ratios described above, only in the tails of the charged particle multiplicity distributions do the extracted parameters vary from the general trend.

The measured multiplicity and charge distributions presented in Figs. 1–7 are sensitive to the acceptance of the experimental apparatus. While it is impossible to determine all experimental biases completely, the hybrid model calculations described in Sec. IV have been used to investigate how the response of the apparatus influences the measurements. Because of the large momentum of the ^{129}Xe projectile, the model calculations indicate that the energy thresholds of the apparatus have a negligible effect on the measured distributions. The incomplete acceptance is due mainly to an incomplete solid angle coverage, and deviations in acceptance exist because of a varying coverage as a function of scattering angle. The Si detector array, which is situated at laboratory angles of 2°–16°, has a significantly smaller geometric acceptance than does the Miniball, which covers larger angles. Hence reaction products which are forward focused have smaller detection efficiencies than products which are distributed more isotropically.

Model calculations for central collisions give charged particle detection efficiencies that vary only slightly from ~75% for the ^{129}Xe+^{197}Au system to ~70% for the ^{129}Xe+^{27}Al system. However, because of the large c.m. velocity in the ^{129}Xe+^{27}Al reaction, the emitted fragments become much more forward focused with increasing charge. Calculations for this reaction indicate that the detection efficiencies decrease from ~70% for $Z=3$ fragments to ~60% for $Z=10$ fragments.

Applying such an efficiency correction decreases the extracted α parameters by ~5% in Fig. 7, but does not change the conclusions drawn from the plot. Fragments with $Z>10$ could be expected to have even smaller detection efficiencies in the asymmetric reactions; however, these fragments do not contribute significantly to the measured multiplicities and hence will not affect the target systematics shown in Figs. 2–5.

In Fig. 8 the experimental energy distributions (solid circles) for C fragments emitted in the ^{129}Xe+^{197}Au reaction are plotted for scattering angles from 11.4° to 90°. These distributions are gated on central collisions ($b\le 0.3b_{\rm max}$) in order to select events in which there is a maximum degree of equilibration. The spectra at for-

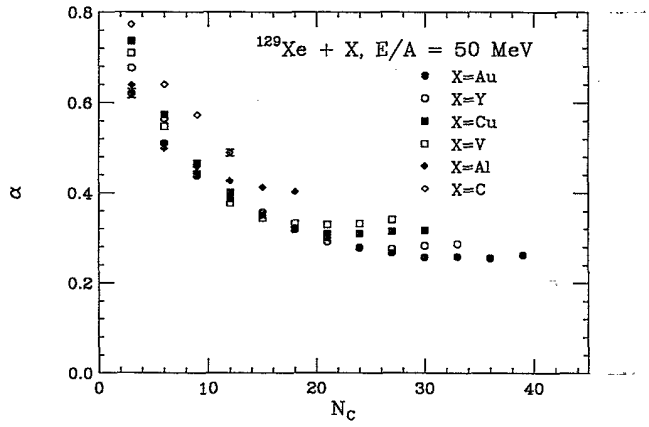

FIG. 7. Parameters of exponential ($e^{-\alpha Z}$) fits to the measured charge distributions ($Z=3$–10) for the $E/A=50$ MeV ^{129}Xe+^{197}Au, ^{89}Y, ^{nat}Cu, ^{51}V, ^{27}Al, and ^{12}C reactions as a function of total charged particle multiplicity N_c. The different symbols represent the indicated targets.

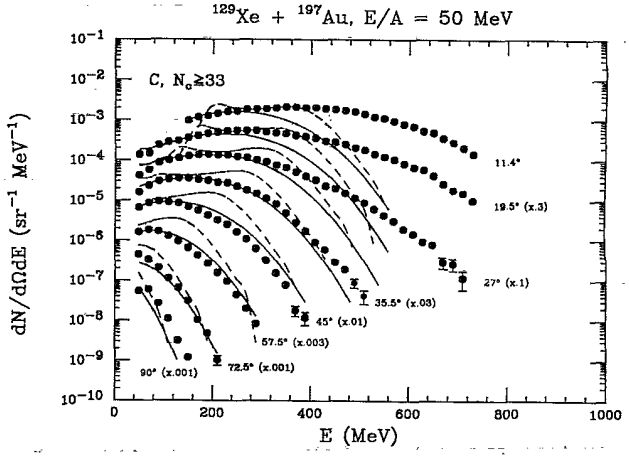

FIG. 8. Energy distributions of carbon fragments emitted in $E/A=50$ MeV ^{129}Xe+^{197}Au collisions for a central impact parameter gate ($N_c\ge 33$, $b\le 0.3b_{\rm max}$). The solid circles correspond to the experimental data at the indicated scattering angles. The solid lines show distributions predicted by the source fit described in the text. The dashed lines show predictions of the hybrid model.

ward angles $<35.5°$ have high-energy tails which extend to energies far beyond the beam energy per nucleon (600 MeV). The distributions for scattering angles $<72.5°$ show very broad maxima. The corresponding angular distribution for $Z=6$ fragments in the same reaction is shown in Fig. 9. The measured differential cross sections decrease nearly exponentially between 4° and 150°.

Previous inclusive studies in this energy regime have indicated that a large fraction of the IMF's are emitted in nonequilibrium process [30–34]. However, in these investigations a selection on the violence of the collision was impossible. To investigate quantitatively the degree to which a single equilibrated source can reproduce the multiplicity-gated energy spectra, we have performed a simple moving source fit to the measured distributions. The parametrization assumes volume emission from a single moving source:

$$\frac{dN(E,\theta)}{dE\,d\Omega}=N_0\left[\frac{E(E_{\text{c.m.}}-V_C)}{E_{\text{c.m.}}}\right]^{1/2}e^{-(E_{\text{c.m.}}-V_c)/T}, \quad (2)$$

where

$$E_{\text{c.m.}}=E+E_0-2(EE_0)^{1/2}\cos\theta \quad (3)$$

and E_0 is the laboratory energy of a fragment at rest in the moving frame, $E_0=mv_0^2/2$. In this parametrization the Coulomb barrier V_C moves along with the source. Systems which decay from an extended nuclear volume, or undergo a significant amount of sequential decay, can be emitted with a range of Coulomb barriers. To allow for these effects, we have provided for a Gaussian smearing of the Coulomb barrier parameter V_C:

$$P(V_C)=(2\pi\sigma_v^2)^{-1/2}\exp[-(V_C-V_X)^2/2\sigma_v^2]\,. \quad (4)$$

The velocity of the moving frame was fixed at a value equal to the center-of-mass velocity, $v_0=0.129c$. Similarly, the temperature T of the emitting source was fixed at a value of 10 MeV, derived from the center-of-mass energy using the Fermi-gas equation $T=(E_{\text{c.m.}}/a)^{1/2}$ and a level-density parameter of $a=8.5$ MeV^{-1}. This left three adjustable fitting parameters: the normalization parameter N_0 and the Coulomb barrier parameters V_X and σ_v. The values extracted by the fitting procedure were $N_0=2.85\times10^{-3}$ sr^{-1}MeV$^{-3/2}$, $V_X=37.5$ MeV, and $\sigma_v=45$ MeV.

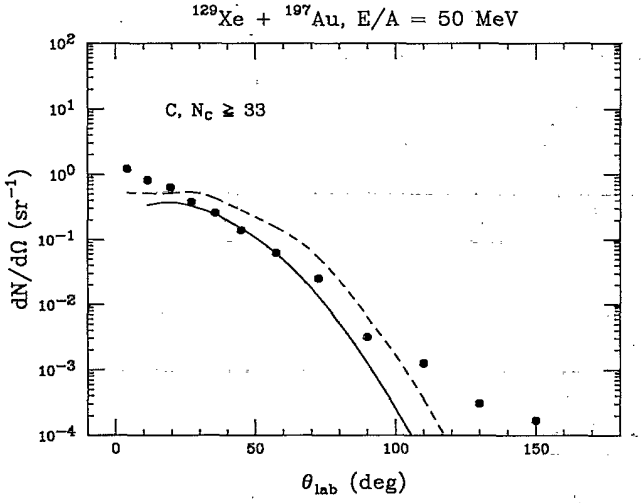

FIG. 9. Angular distributions of carbon fragments emitted in $E/A=50$ MeV ^{129}Xe+^{197}Au collisions for a central impact parameter gate ($N_c\geq33$, $b\leq0.3b_{\text{max}}$). The solid circles correspond to the experimental data. The solid curve is the distribution predicted by the source fit described in the text. The dashed curve is predicted by the hybrid model.

Results of the fits are shown as the solid and dashed lines in the upper panel of Fig. 8 and the solid line in Fig. 9. For scattering angles between 35.5° and 72.5°, the fits are good. At more forward and more backward angles, the single source fit underpredicts the measured cross sections for the more energetic fragments. This may indicate an incomplete stopping of the projectile nucleons by the target and vice versa. However, the bulk of the experimental yield occurs in the angular range in which the fit essentially reproduces the data. In fact, the single moving source predicts ~90% of the measured C fragment yield. This stands in contrast to studies of asymmetric reactions without impact parameter selection [30–34], where energy spectra and angular distributions indicate that the bulk of the fragment yield must be attributed to nonequilibrium processes.

The extracted Coulomb barrier parameters $V_X=37.5$ MeV and $\sigma_v=45$ MeV indicate emission over a very broad range of Coulomb barriers. A lowering and broadening of the effective emission barriers for fragment emission have previously been observed in high-energy reactions [48–50]. Such effects for light particle emission have been attributed to decay from an expanded nuclear volume [51], to a substantial amount of sequential emission [52], or to thermally induced barrier fluctuations [22,53]. Each of these effects could be pronounced in the most violent ^{129}Xe+^{197}Au collisions in which the average IMF multiplicity is >6.

The maximum Coulomb energy should be nearly the binary emission energy of C fragments from a composite system of $Z=133$ and $A=326$. Only a small fraction of the Coulomb barriers considered in the fit should exceed this energy. Empirically, fragment emission energies are well described by the formula

$$E_{\text{Coul}}=1.44Z_1Z_2/[r_0(A_1^{1/3}+A_2^{1/3})+2]\,, \quad (5)$$

with a radius parameter $r_0=1.2$ fm [54]. This formula predicts a Coulomb barrier for C emission of 81.9 MeV after correcting for the recoil energy. For fitting parameters of $V_X=37.5$ MeV and $\sigma_v=45$ MeV, only 16% of the fragments are emitted with Coulomb barriers >81.9 MeV; thus, these parameters are not inconsistent with the empirical value.

IV. THEORETICAL CALCULATIONS

A. Models employed

To model the early stage of the collision, we have performed calculations with the microscopic BUU transport equation [39], which describes the temporal evolution of

the one-body density. The BUU equation is expected to give a reasonable description of preequilibrium nucleon emission and of global quantities such as intrinsic excitation energies and collective expansion velocities on time scales of ~ 100 fm/c. For longer time scales, BUU becomes unrealistic because it cannot make reliable predictions about cluster emission, which becomes particularly important when the system expands to low density. In these later stages of the reaction, statistical treatments may be more appropriate. We therefore follow the time evolution during the later stages of the reaction using the EES model, which incorporates the statistical emission of intermediate mass fragments [29].

The BUU equation [39]

$$\begin{aligned}\partial_t f(\mathbf{p},\mathbf{r},t)+(\mathbf{p}/m)\cdot\nabla_r f(\mathbf{p},\mathbf{r},t)-\nabla_r U(r)\cdot\nabla_p f(\mathbf{p},\mathbf{r},t)\\ =\tfrac{1}{2}\pi^3 m^2\int d^3q_1' d^3q_2 d^3q_2' \delta\{\tfrac{1}{2}m(p^2+q_2^2+q_1'^2+q_2'^2)\}\delta(\mathbf{p}+\mathbf{q}_2-\mathbf{q}_1'-\mathbf{q}_2')\frac{d\sigma}{d\Omega}\\ \times\{f(\mathbf{q}_1',\mathbf{r},t)f(\mathbf{q}_2',\mathbf{r},t)[1-f(\mathbf{p},\mathbf{r},t)][1-f(\mathbf{q}_2',\mathbf{r},t)]\\ -f(\mathbf{p},\mathbf{r},t)f(\mathbf{q}_2',\mathbf{r},t)[1-f(\mathbf{q}_1',\mathbf{r},t)][1-f(\mathbf{q}_2',\mathbf{r},t)]\}\end{aligned} \tag{6}$$

was solved numerically using a parallel ensemble method, with each nucleon represented by 90 test particles. The phase-space density of nucleons, $f(\mathbf{p},\mathbf{r},t)$, propagates under the joint influence of a nuclear potential, a Coulomb potential, and a nucleon-nucleon collision term. The in-medium nucleon-nucleon scattering cross section $d\sigma/d\Omega$ was assumed to be proportional to the experimentally determined (energy-dependent) cross section for free nucleons, $d\sigma_{NN}/d\Omega$. Two density-dependent Skyrme parametrizations were chosen to approximate the nuclear mean field:

$$U=a(\rho/\rho_0)+b(\rho/\rho_0)^\sigma . \tag{7}$$

With $a=-124$ MeV, $b=70.5$ MeV, and $\sigma=2$, the parametrization corresponds to a compressibility coefficient of $K_\infty=380$ MeV ("stiff" equation of state); with $a=-356$ MeV, $b=303$ MeV, and $\sigma=\frac{7}{6}$, the parametrization corresponds to a compressibility coefficient of $K_\infty=210$ MeV ("soft" equation of state). The normal nuclear matter density ρ_0 is taken to be 0.168 fm^{-3}.

In the BUU calculations, the integrated mass loss $A_{\rm loss}$ is calculated by evaluating the local nucleon number density in a cubic cell of volume 1 fm^3 around each nucleon. Nucleons for which the local density is less than $\frac{1}{8}$ of normal nuclear density are considered to be unbound.

The average density of the residue predicted by the BUU model is calculated by averaging over the local densities of all bound nucleons. The binding energy of a residue of $A_{\rm res}$ nucleons can be approximated as

$$E_{\rm binding}=-\sum_{i=1}^{A_{\rm res}}\left[\mathbf{p}_i^2/2m+(e^2/2)\sum_{j\neq i}|\mathbf{r}_i-\mathbf{r}_j|^{-1}+\tfrac{1}{2}a[\rho(\mathbf{r}_i)/\rho_0]+b\rho(\mathbf{r}_i)^\sigma/\rho_0^\sigma(\sigma+1)\right], \tag{8}$$

where a, b, σ, and ρ_0 are defined from the Skyrme parametrization above (7), $e^2=1.44$ MeV fm, and $\rho(\mathbf{r}_i)$ is the local density of particle i. The excitation energy of the residue can then be determined from $E^*=E_{\rm LD}-E_{\rm binding}$, where $E_{\rm LD}$ is the liquid-drop binding energy of a collection of $A_{\rm res}$ nucleons.

The EES model characterizes an ensemble of emitting sources by a time-varying average density $\rho(t)$ to which the level densities of the source are related. For the purpose of calculating the mean collective expansion energy, the model assumes, in addition, that the density of the source is uniform. This assumption requires that the collective radial velocity increase linearly with radius. The radial expansion energy E_r is then given by

$$E_r=\tfrac{1}{2}mA_{\rm res}\left[\frac{dR_{\rm rms}}{dt}\right]^2 . \tag{9}$$

Here m is the mass of a nucleon and $dR_{\rm rms}/dt$ is the time derivative of the root-mean-squared radius. To optimize the connection between the BUU and the expanding compound nucleus models, we take Eq. (9) to describe the collective energy of expansion in the BUU model as well. The time derivative of the root-mean-squared radius can be calculated in the BUU model as

$$\frac{dR_{\rm rms}}{dt}=\sum_{i=1}^{A_{\rm res}}\frac{\mathbf{r}_i\cdot\mathbf{p}_i}{mA_{\rm res}R_{\rm rms}} , \tag{10}$$

where $\mathbf{r}_i$ and $\mathbf{p}_i$ are the positions and momenta of the test particles in the center-of-mass system.

In the EES model, the dynamical response of the source is governed by the interplay of thermal pressure and the nuclear binding forces, which tend to return the density to its equilibrium value ρ_0. The binding effects are provided by the finite-nucleus compressibility. For simplicity, the binding energy per nucleon at densities different from ρ_0 is assumed to deviate from liquid-drop values by a quadratic function of density,

$$E(\rho)/A=E_{\rm LD}(\rho_0)/A+(K/18)(1-\rho/\rho_0)^2 , \tag{11}$$

where K is the finite-nucleus compressibility coefficient. This compressibility includes surface and Coulomb effects and, hence, differs from the infinite-matter compressibility K_∞, which is used in the BUU calculations.

It is instructive to compare the time evolution of the

composite systems predicted by the two models. Figures 10–12 depict the predicted temporal evolution of the integrated mass loss ($A_{\rm loss}$, top panel), average density ($\langle\rho_{\rm res}\rangle$, middle panel), and the collective radial energy in the residue (E_r/A, bottom panel). Figures 10 and 11 show the results of BUU calculations for the $E/A=50$ MeV ^{129}Xe+^{27}Al, ^{51}V, ^{89}Y, and ^{197}Au reactions using $K_\infty=380$ and 210, respectively [55]. Figure 12 presents a sample EES calculation [29] for the expansion and decay of a source with a finite-nucleus compressibility of $K=200$ MeV using initial values of $Z=133$, $A=326$, normal nuclear matter density, a temperature of $T=12$ MeV, and a collective radial energy of 100 MeV. At $t=0$ the EES calculations begin with an excited system expanding from normal nuclear matter density, while the surfaces of the projectile and target nuclei are separated by 4 fm in the BUU calculations and do not reach normal nuclear density until about 35–45 fm/c later. Hence there is an effective offset of approximately +40 fm/c in the time scale of the expanding compound nucleus calculations in Fig. 12.

The predicted rate of mass loss is qualitatively similar for both sets of calculations. The mass loss becomes important following a time of $t\approx40$ fm/c in the BUU calculations and $t=0$ fm/c in the EES calculations, when the systems begin to expand. At later times the calculated emission rates decreases; this effect is manifested by a decreasing slope in the time dependence of $A_{\rm loss}$. The gradual decrease of the emission rates with time is related to the decrease in excitation energy as the systems cool. In contrast, the fragment emission rate ($N_{\rm IMF}$, left scale in Fig. 12) in the EES model sharply increases when the system approaches a minimum in density. Approximately one-half of the total IMF yield occurs between 40 and 70 fm/c, near the first density minimum.

In both sets of calculations, the systems undergo density oscillations. For the BUU calculations with heavier targets, the minimum densities reached are about $\frac{1}{2}$ of the original density [56] and are rather similar to the minimum density reached in the EES calculations. In the early stages of the BUU calculations, the collective radial energy is trivially dominated by the relative velocity of the projectile and target. At the point of maximum compression, the BUU calculations predict a complete damping of the relative motion of projectile and target, and the collective radial energy vanishes. During the

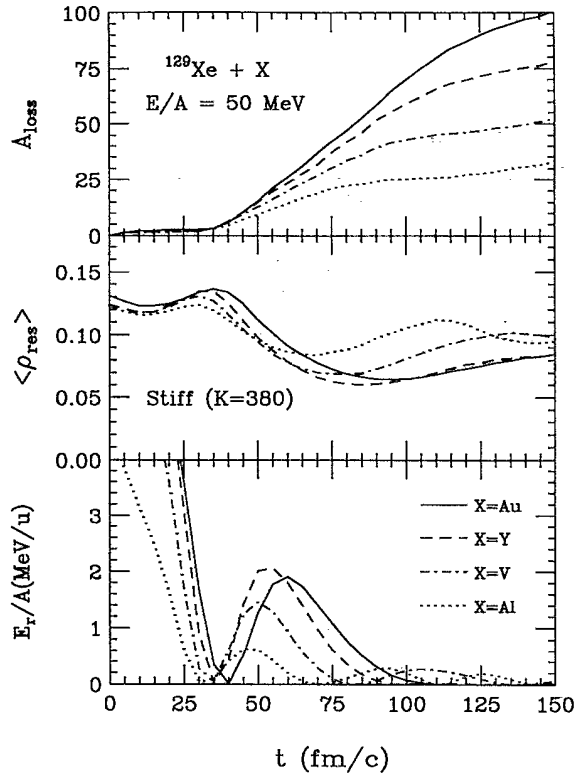

FIG. 10. Results of BUU calculations for $E/A=50$ MeV ^{129}Xe+^{197}Au, ^{89}Y, ^{51}V, and ^{27}Al reactions with a stiff ($K_\infty=380$ MeV) equation of state. The mass loss ($A_{\rm loss}$, top panel), average density of the residue of bound test particles ($\langle\rho_{\rm res}\rangle$, second panel), excitation energy per nucleon of the residue (E^*/A, third panel), and collective radial energy per nucleon of the residue (E_r/A, bottom panel) are plotted as a function of time. The solid, dashed, dot-dashed, and dotted curves correspond to calculations for the ^{197}Au, ^{89}Y, ^{51}V, and ^{27}Al targets, respectively.

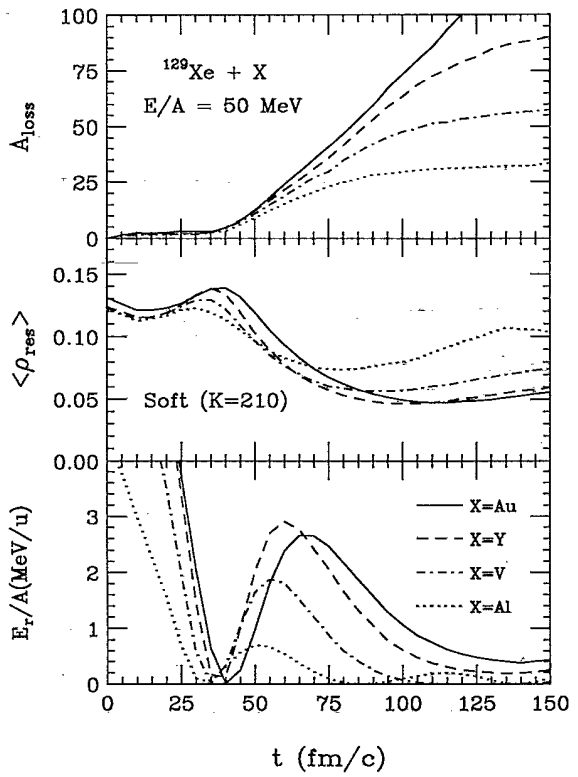

FIG. 11. Results of BUU calculations for $E/A=50$ MeV ^{129}Xe+^{197}Au, ^{89}Y, ^{51}V, and ^{27}Al reactions with a soft ($K_\infty=210$ MeV) equation of state. The mass loss ($A_{\rm loss}$, top panel), average density of the residue of bound test particles ($\langle\rho_{\rm res}\rangle$, second panel), excitation energy per nucleon of the residue (E^*/A, third panel), and collective radial energy per nucleon of the residue (E_r/A, bottom panel) are plotted as a function of time. The solid, dashed, dot-dashed, and dotted curves correspond to calculations for the ^{197}Au, ^{89}Y, ^{51}V, and ^{27}Al targets, respectively.

subsequent expansion phase, the BUU calculations predict the collective radial energy to reach values of 1–3 MeV/nucleon before dissipating. The calculated values of the radial kinetic energy depend upon the equation of state used in the calculations. The soft [$K_\infty = 210$ MeV (Fig. 11)] equation of state allows more energy to be transferred into collective radial motion than the stiff [$K_\infty = 380$ MeV (Fig. 12)] equation of state. The maximum values calculated for the ^{129}Xe+^{197}Au system are about 2 MeV/nucleon for the stiff equation of state and about 3 MeV/nucleon for the soft equation of state. In the EES calculation shown in Fig. 12 for a similar mass system, the collective radial energy oscillates between 0.8 MeV/nucleon during expansion or compression and 0 near the turning points.

While the microscopic BUU model allows anisotropic density distributions and damping of the collective radial energy into thermal excitation energy, the density calculated with the EES model undergoes an oscillation with a period of approximately 110 fm/c and little damping of the radial collective energy into thermal energy. The persistance of large radial kinetic energies on long time scales in the EES calculation does not affect the calculated fragment multiplicities greatly, since most of the fragment emission is predicted to occur early in the calculation.

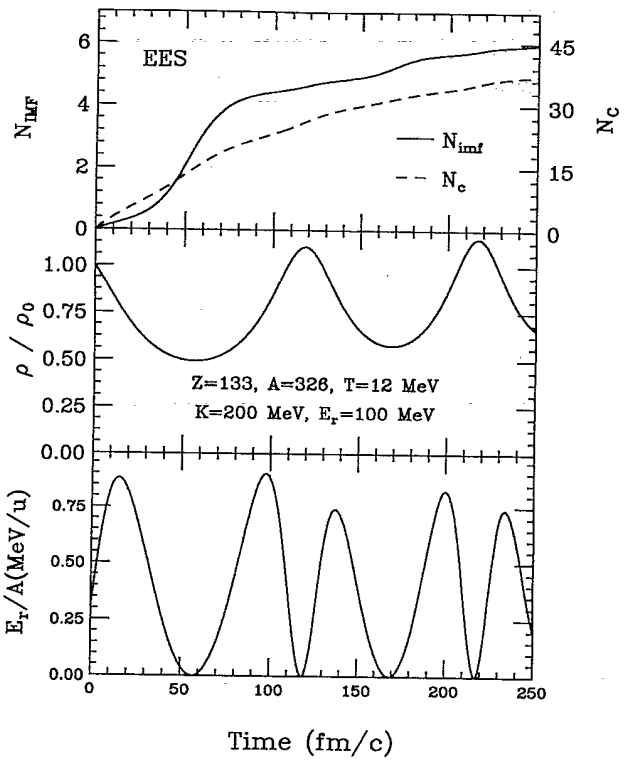

FIG. 12. Results of the expanding compound nucleus model calculations for an initial system with $Z = 133$, $A = 326$, a temperature $T = 12$ MeV, and a collective radial energy $E_r = 100$ MeV. The calculations were performed with a finite-nucleus compressibility $K = 200$ MeV. The integrated yield of IMF's (N_{IMF}, solid curve) and total charged particles (N_c, dashed curve) are shown in the top panel as functions of time. The density relative to normal nuclear density (ρ/ρ_0, second panel), the excitation energy per nucleon (E^*/A, third panel), and the collective radial energy of the residue (E_r/A, bottom panel) are shown in the other panels as functions of time.

B. Matching the models

We use the BUU calculations to describe the early phase of the collisions, i.e., the initial compression and deposition of energy. The EES model is used to describe the later phase of the reactions involving fragment emission. The EES model requires input values for four quantities: the source mass, the source charge, the radial kinetic energy, and the thermal excitation energy. The initial value of the density is taken to be normal nuclear matter density. We choose to couple the BUU calculations with the EES calculations at the time following initial compression when the calculated radial density distributions correspond most nearly to normal nuclear matter distributions. This condition seems to be relatively easy to determine.

For illustration, Figs. 13 (stiff equation of state) and 14 (soft equation of state) show density distributions predicted by the BUU equation at five equally spaced time steps for the $E/A = 50$ MeV ^{129}Xe+^{197}Au, ^{89}Y, ^{51}V, and ^{27}Al reactions. The times corresponding to the two extreme time steps are given alongside the upper and lower curves. The nuclear saturation density ρ_0 is indicated by the long-dashed line in each figure. Each density distribution resembles a Fermi distribution with a interior region of constant density and a finite surface region where

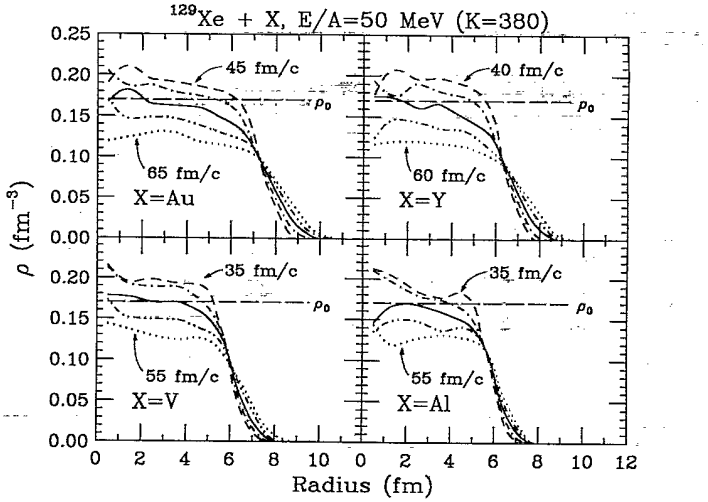

FIG. 13. Density distributions for $E/A = 50$ MeV ^{129}Xe+^{197}Au, ^{89}Y, ^{51}V, and ^{27}Al reactions as calculated with the BUU model using a stiff ($K_\infty = 380$ MeV) equation of state. Each panel is labeled by target. The top (dashed) curve in each panel corresponds to the time step indicated in the upper right of the panel; the bottom (dotted) curve corresponds to the time step indicated in the lower left. The three intermediate curves correspond to times of +5 fm/c (dot-dashed, second from top), +10 fm/c (solid, third), and +15 fm/c (dot-dot dashed, fourth) after the upper curve. Nuclear saturation density is indicated by the long-dashed line in each figure denoted as ρ_0.

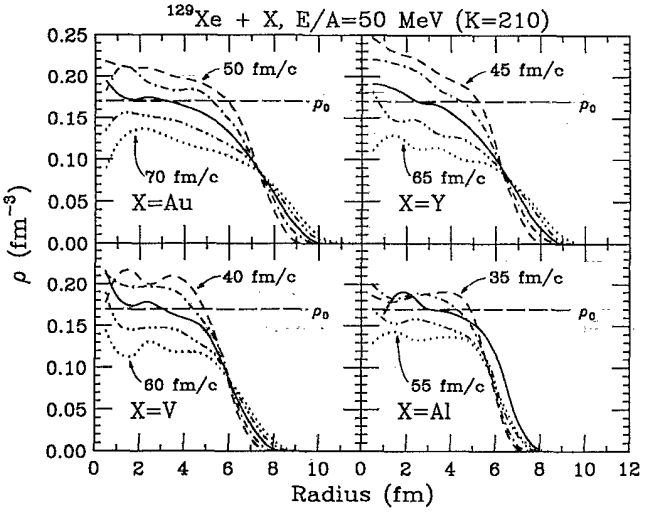

FIG. 14. Density distributions for $E/A=50$ MeV ^{129}Xe+^{197}Au, ^{89}Y, ^{51}V, and ^{27}Al reactions as calculated with the BUU model using a soft ($K_\infty=210$ MeV) equation of state. Each panel is labeled by target. The top (dashed) curve in each panel corresponds to the time step indicated in the upper right of the panel; the bottom (dotted) curve corresponds to the time step indicated in the lower left. The three intermediate curves correspond to times of +5 fm/c (dot-dashed, second from top), +10 fm/c (solid, third), and +15 fm/c (dot-dot dashed, fourth) after the upper curve. Nuclear saturation density is indicated by the long-dashed line in each figure denoted as ρ_0.

the density decreases to zero. We observe a smooth evolution in time from compressed systems (upper two curves), through a system near equilibrium density (middle, solid curve), and finally to systems at low density (bottom two curves). For each reaction we have chosen to match the two models when the calculated interior density is closest to nuclear saturation density. These times are given in Table I.

The BUU calculations suggest that a necessary condition for the use of statistical models is indeed achieved at the time at which the systems have returned to normal nuclear density; i.e., the mean radial motion becomes nearly isotropic. Very early in the collision the collective radial motion is large and predominately directed parallel to the beam direction. Prior to reaching the matching time at $\rho=\rho_0$, the radial motion perpendicular to the beam has grown to represent about $\frac{2}{3}$ of the total radial kinetic energy, consistent with requirements for thermal models. Since collective kinetic energy persists at longer times, full thermalization is not achieved. The collective kinetic energy can, however, be incorporated into the EES calculations.

The mass of the decaying residue must be determined from the BUU calculation. This choice is complicated because it is difficult to clearly distinguish particles near the nuclear surface which are a part of the residue from those which are unbound. In order to choose reasonable values for the mass of the residue, we have investigated the radial distributions of the density, the excitation energy per nucleon, and the collective radial velocity, as calculated with the BUU model at the selected coupling time.

In Fig. 15 we have plotted, for two particular reactions, the density, binding energy per nucleon, and radial velocity for spherical shells of thickness 1 fm at the times given in Table I. The density distributions, given previously in Fig. 14, are shown again for convenience. In the middle panel, the binding energies per nucleon are plotted as a function of radius. These binding energies are

TABLE I. Input parameters for the statistical model calculations as determined from microscopic BUU calculations. The BUU calculations were performed for $E/A=50$ MeV ^{129}Xe-induced reactions on four different targets and for two values of the compressibility parameter $K_\infty=380$ ("stiff") and $K_\infty=210$ ("soft"). Listed is the time at which the BUU and statistical model calculations were matched (t), the radius (r), charge (Z), mass (A), excitation energy per nucleon (E^*/A), temperature (T) [58], collective radial energy of the residue (E_r), and the number of emitted charges in the preequilibrium (BUU) phase (ΔZ).

Target K_∞	t (fm/c)	r (fm)	Z	A	E^*/A (MeV)	T (MeV)	E_r (MeV)	ΔZ
^{27}Al, stiff	45	6	54	127	2.477	5.69	61.5	13
	45	7	63	147	3.536	6.93	88.5	4
^{51}V, stiff	45	6	56	137	4.984	8.42	110.4	21
	45	7	69	165	5.828	9.23	182.1	8
^{89}Y, stiff	50	7	75	180	6.099	9.48	290.8	18
	50	8	84	200	6.841	10.15	389.3	9
^{197}Au, stiff	55	8	108	271	6.188	9.56	394.6	25
	55	9	120	300	6.855	10.17	510.6	13
^{27}Al, soft	45	6	54	129	2.433	5.63	53.7	13
	45	7	63	148	3.112	6.45	79.5	4
^{51}V, soft	50	6	54	130	3.238	6.59	133.2	23
	50	7	67	159	4.194	7.63	230.4	10
^{89}Y, soft	55	7	70	170	4.412	7.85	380.2	23
	55	8	82	196	5.190	8.62	507.6	11
^{197}Au, soft	60	8	103	260	4.666	8.11	485.5	30
	60	9	118	293	5.286	8.72	655.3	15

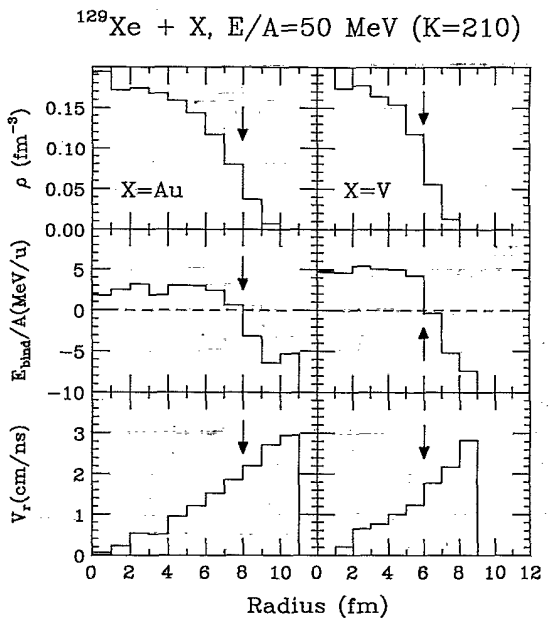

FIG. 15. Results of BUU calculations for $E/A=50$ MeV ^{129}Xe+^{197}Au (left panels) and ^{51}V (right panels) with a soft ($K_\infty=210$ MeV) equation of state. The density (top panels), binding energy per nucleon (middle panels), and collective radial velocity (bottom panels) are plotted for spherical shells of thickness 1 fm at the collision times of 60 fm/c (^{197}Au target) and 50 fm/c (^{51}V target). The dashed lines in the middle panels delineate shells that are bound on the average from those that are unbound. The arrows indicate radial cuts which include only those shells that have an average positive binding.

about 2–3 MeV/nucleon for the ^{129}Xe+^{197}Au system and 4–5 MeV/nucleon for the ^{129}Xe+^{51}V system for nucleons in the nuclear interior. Nucleons in the outer shells with densities <0.06 fm^{-3} are unbound on the average. This occurs for radii >8 fm for the ^{129}Xe+^{197}Au system and for radii >6 fm for the ^{129}Xe+^{51}V system. A large fraction of the nucleons in these unbound shells are eventually emitted as preequilibrium particles and should not be considered as part of the residue. (The inclusion of such unbound test particles in the residues would lead to artifically large values of E^* and E_r, and therefore to artificially increased fragment multiplicities.) To assess the resulting uncertainties in determining the residue mass, we have performed one set of statistical model calculations with initial conditions calculated using only bound shells. These radial cuts are indicated by the arrows in Fig. 15. Since the first unbound shell also includes a significant fraction of bound nucleons (typically $\approx 50\%$), we have performed a second set of calculations including the first unbound shell as well [57].

In the bottom panel of Fig. 15, the average radial velocity of each shell is plotted as a function of radius. For shells with net positive binding, the radial velocity exhibits a nearly linear increase with r, consistent with isotropic expansion as assumed in the statistical expanding compound nucleus model [29]. This lends further confidence in the matching procedure that we employ.

Having selected the coupling time and the mass and charge of the decaying residue, we find the excitation energy for the EES calculations from the binding energy following Eq. (8) and the radial kinetic energy of expansion using Eq. (9).

C. Comparison with data

The charges, masses, excitation energies per nucleon, temperatures [58], and collective radial velocities of the residues deduced from the results of the BUU calculations are given in Table I for the four different systems, two different equations of state, and the two radial cutoffs. These source parameters were used as input for the expanding compound nucleus model calculations. The results of these sets of calculations are compared in Fig. 16 to experimental data (solid circles) for central ($b<0.3b_{max}$) gates on impact parameter as determined from the charged particle multiplicity distributions. In comparing with the data, the total amount of emitted preequilibrium charge was taken to be the amount of charge beyond the radial cutoffs in the BUU calculations. In order to convert this calculated preequilibrium charge into a charged particle multiplicity, we have divided by the average charge per detected light charged particle ($Z=1,2$) as observed in central collisions ($b<0.3b_{max}$) for each system (see Table II).

Four sets of calculations are represented by the bounded areas in each panel of Fig. 16. The vertically hatched areas correspond to calculations with the larger radial

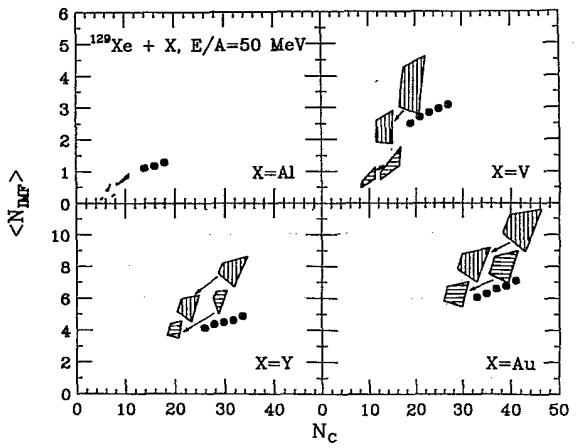

FIG. 16. Comparison of the experimental and theoretical ratios between the average IMF multiplicity $\langle N_{IMF}\rangle$ and the total charged particle multiplicity N_c for $E/A=50$ MeV ^{129}Xe+^{197}Au, ^{89}Y, ^{51}V, and ^{27}Al reactions. The panels are labeled by target. Solid points correspond to experimental results for central impact parameters ($b\leq 0.3b_{max}$). The right (left) sides of the hatched regions in each panel correspond to microscopic model calculations with a stiff (soft) equation of state, $K_\infty=380$ (210) MeV. The bottom (top) of each hatched region corresponds to EES calculations with a finite-nucleus compressibility of $K=250$ (144) MeV. Horizontal hatching indicates calculations with the smaller radial cutoff and vertical hatching calculations with the larger radial cutoff. The effect of filtering by the experimental acceptance is shown by the arrows between regions with similar hatching.

TABLE II. Average charge of light charged particles ($Z=1,2$) detected for central ($b<0.3b_{max}$) events in $E/A=50$ MeV ^{129}Xe-induced reactions.

Target	N_c	$\langle Z_{LP}\rangle$
^{197}Au	≥ 33	1.42
^{89}Y	≥ 25	1.41
^{51}V	≥ 19	1.39
^{27}Al	≥ 14	1.34

cutoffs; the horizontally hatched areas correspond to calculations with the smaller radial cutoffs. The effect of filtering the theoretical calculations through a software replica of the experimental device is illustrated by the sets of arrows in each subplot. The sensitivity to the equation of state used in the BUU calculations is shown by the horizontal extent of each individual bounded area; the sensitivity to the finite-nucleus compressibility coefficient used in the expanding compound nucleus calculations is indicated by the vertical extent of each individual area.

In greater detail each area was obtained as follows: Calculations performed with a stiff equation of state ($K_\infty=380$ MeV) in the microscopic model correspond to the right boundary of each area, and calculations performed with a soft equation of state ($K_\infty=210$ MeV) correspond to the left boundary. This parameter's sensitivity can be understood as follows: With a stiff equation of state, the calculated initial excitation energies and temperatures are larger than with a soft equation of state (see Table I). Larger temperatures give rise to larger total charged particle multiplicities; hence, the calculations move nearly horizontally. The multiplicities of intermediate mass fragments are not greatly affected by the different equations of state during the compressional phase.

The sensitivities to the finite nucleus compressibility K of the expanding compound nucleus model calculations are indicated by the curves corresponding to the upper and lower bounds of the areas. Calculations performed with $K=250$ MeV provide the lower boundary, and calculations performed with $K=144$ MeV represent the upper boundary. This parameter's sensitivity can be understood as follows: The compressibility in the expansion phase has a very strong effect on the calculated fragment multiplicity, but only a small effect on the total charged particle multiplicity. Softer equations of state lead to less dense systems and to enhanced fragment emission.

The vertically hatched areas represent calculations with the larger radial cutoff (marked by the arrows in Fig. 15), and the horizontally hatched areas represent calculations with the smaller radial cutoff. The inclusion of the first unbound shell strongly increases the average fragment multiplicity, but only weakly increases the total charged particle multiplicity. This can be understood by noting that the inclusion of an additional shell causes only a small increase in the temperatures ($<10\%$), but a much larger increase in the collective radial energy ($>25\%$—see Table I), since, as was shown above, E_r is nearly proportional to the radius. A larger collective radial energy will lead to more expanded systems and, hence, to significantly larger fragment multiplicities.

The effect of filtering is shown by the arrows between the two sets of hatched regions. Regions to the right correspond to unfiltered calculations and those to the left to filtered calculations. The filtering was performed by considering the energy and angular distributions of the preequilibrium particles as calculated using the BUU model and the total multiplicity, charge, and energy distributions of the evaporated particles as calculated with the expanding compound nucleus model. A total of 10 000 events was simulated for each set of input parameters and filtered through a software replica of the experimental device, which takes into account energy thresholds, angular acceptances, and double-hit probabilities. Filtering acts to decrease both the total charged particle and intermediate mass fragment multiplicities in about equal proportions, so that the $\langle N_{IMF}\rangle/N_c$ ratios of the filtered and unfiltered calculations are not changed appreciably.

The general agreement between the sets of filtered calculations and the data is fair. Given the excitation energies and radial kinetic energies from the microscopic model calculations, the EES calculations are able to predict average fragment multiplicities that are in reasonable agreement with the data. However, the total number of charge particles predicted theoretically is systematically less than observed experimentally. This agreement is influenced by our assumptions about the number of emitted preequilibrium particles. Different assumptions (all $Z=1$ particles, for instance) may lead to larger theoretical multiplicities and to better agreement between data and theory. The sequential decay of excited fragments, which is not treated in the EES, will also lead to an increase in N_c.

While the number of intermediate mass fragments predicted for the ^{129}Xe+^{197}Au, ^{89}Y, and ^{51}V system is in reasonable agreement with the data, the fragment multiplicity predicted for the ^{129}Xe+^{27}Al system is too low. There are several possible explanations for this discrepancy. The BUU calculations provide only the average excitation energy $\langle E^*\rangle$ in a given collision, and fragment multiplicity is a nonlinear function of excitation energy. For a given reaction geometry, excitation energies larger than $\langle E^*\rangle$ give the most important contributions to the average fragment multiplicity. This effect is more pronounced for systems with lower excitation energies. For such a system, ^{129}Xe+^{27}Al, we find the greatest discrepancy between experiment and theory.

Alternatively, the BUU calculations for the ^{129}Xe+^{27}Al system indicate that the temperature and collective radial energy are too small for significant expansion to occur. Transition-state model calculations have shown that, for systems at normal nuclear density and rather low excitation energy, fragment emission is enhanced at high angular momentum [54]. If the charged particle multiplicity gate for this reaction does not adequately suppress large angular momentum collisions, rapidly rotating compound nuclei may be found. Decay from these systems may lead to enhancements in fragment multiplicity which are not considered in the EES model.

Finally, in Figs. 8 and 9, we consider the energy spec-

tra and angular distribution of carbon fragments as calculated with the hybrid model for the $^{129}Xe+^{197}Au$ reaction. The dashed curves in Fig. 8 correspond to calculations using a compressibility of $K_\infty=210$ MeV in the BUU calculation, and radial extent of 9 fm for the emitting source, and a finite-nucleus compressibility of $K=144$. The dashed curve in Fig. 9 is the corresponding angular distribution calculated with the same set of parameters. The model calculations are very similar to the single source fits described in Sec. III. The calculations do not predict the tails of the energy distributions at the most forward and backward angles; however, the shapes of the energy spectra are well reproduced for intermediate angles between 35.5° and 72.5° where the bulk of the yield is observed. For this set of input parameters, the total cross section for C fragments is overpredicted by approximately 70%; however, other sets of parameters with larger values of K_∞ and K, or a smaller source radius, give better agreement with the observed C yield.

V. SUMMARY

We have studied intermediate mass fragment multiplicity, charge, energy, and angular distributions for $E/A=50$ MeV $^{129}Xe+^{197}Au$, ^{89}Y, Cu, ^{51}V, ^{27}Al, and ^{12}C reactions using the measured total charged particle multiplicity as a reaction filter. We observe that the fragment multiplicity distributions and charge distributions are strongly dependent upon charged particle multiplicity and show a large degree of target independence. These results, along with the energy and angular distributions observed for high multiplicity $^{129}Xe+^{197}Au$ collisions, suggest that the fragment multiplicity is determined by the excitation energy deposited in the system and that statistical concepts may be useful in calculating the branching ratios for fragment emission.

These data were compared with the results of EES calculations which use input parameters for the excitation energy, radial collective energy, source mass, and source charge supplied by BUU transport model calculations. Overall, the agreement between data and the hybrid model calculations is reasonable, with the exception of the $^{129}Xe+^{27}Al$ system, for which little expansion is predicted. There is a systematic underprediction of the total number of emitted light charged particles. This disagreement may result from assumptions about the nature of preequilibrium particle emission or from neglecting the sequential decay of excited fragments, which is not treated in the expanding compound nucleus model.

The hybrid model calculations indicate that the total charged particle multiplicity is sensitive to the nuclear compressibility in the initial compressional (preequilibrium) phase of the reaction and that the intermediate mass fragment multiplicity is very sensitive to the compressibility in the expansion (statistical decay) phase. Uncertainties in the matching of the two models, specifically in treating preequilibrium decay and in defining the boundary of the equilibrated source, preclude the extraction of precise values for nuclear compressibility parameters. Such a generic limitation of the present hybrid model may also exist for other hybrid approaches. Hence there is a need for more complete models that are able to realistically treat both nonequilibrium and equilibrium emission of both light particles and fragments.

ACKNOWLEDGMENTS

This work was supported by the National Science Foundation under Grant Nos. PHY-86-11210, PHY-89-13815, and PHY-9017077 and the U.S. Department of Energy under Contract No. DE-AC03-76SF00098. W.G.L. acknowledges financial support from the U.S. Presidential Young Investigator Program and N.C. acknowledges partial support by the FAPESP, Brazil.

[1] J. W. Harris, B. V. Jacak, K.-H. Kampert, G. Claesson, K.G. R. Doss, R. Ferguson, A. I. Gavron, H.-A. Gustafsson, H. Gutbrod, B. Kolb, F. Lefebvres, A. M. Poskanzer, H.-G. Ritter, H. R. Schmidt, L. Teitelbaum, M. Tincknell, S. Weiss, H. Wieman, and J. Wilhelmy, Nucl. Phys. **A471**, 241c (1987).

[2] Y. D. Kim, M. B. Tsang, C. K. Gelbke, W. G. Lynch, N. Carlin, Z. Chen, R. Fox, W. G. Gong, T. Murakami, T. K. Nayak, R. M. Ronningen, H. M. Xu, F. Zhu, and W. Bauer, Phys. Rev. Lett. **63**, 494 (1989).

[3] Y. Blumenfeld, N. Colonna, P. Roussel-Chomaz, D. N. Delis, K. Hanold, J. C. Meng, G. F. Peaslee, Q. C. Sui, G. J. Wozniak, and L. G. Moretto, Phys. Rev. Lett. **66**, 576 (1991).

[4] C. A. Ogilvie, J. C. Adloff, M. Begemann-Blaich, P. Bouissou, J. Hubele, G. Imme, I. Iori, P. Kreutz, G. J. Kunde, S. Leray, V. Lindenstruth, Z. Liu, U. Lynen, R. J. Meijer, U. Milkau, W. F. J. Müller, C. Ngo, J. Pochodzalla, G. Raciti, G. Rudolf, H. Sann, A. Schüttauf, W. Seidel, L. Stuttge, W. Trautmann, and A. Tucholski, Phys. Rev. Lett. **67**, 1214 (1991).

[5] D. R. Bowman, G. F. Peaslee, R. T. de Souza, N. Carlin, C. K. Gelbke, W. G. Gong, Y. D. Kim, M. A. Lisa, W. G. Lynch, L. Phair, M. B. Tsang, C. Williams, N. Colonna, K. Hanold, M. A. McMahan, G. J. Wozniak, L. G. Moretto, and W. A. Friedman, Phys. Rev. Lett. **67**, 1527 (1991).

[6] R. T. de Souza, L. Phair, D. R. Bowman, N. Carlin, C. K. Gelbke, W. G. Gong, Y. D. Kim, M. A. Lisa, W. G. Lynch, G. F. Peaslee, M. B. Tsang, H. M. Xu, F. Zhu, and W. A. Friedman, Phys. Lett. B **268**, 6 (1991).

[7] J. Hubele, P. Kreutz, J. C. Adloff, M. Begemann-Blaich, P. Bouissou, G. Imme, I. Iori, G. J. Kunde, S. Leray, V. Lindenstruth, Z. Liu, U. Lynen, R. J. Meijer, U. Milkau, A. Moroni, W. F. J. Müller, C. Ngo, C. A. Ogilvie, J. Pochodzalla, G. Raciti, G. Rudolf, H. Sann, A. Schüttauf, W. Seidel, L. Stuttge, W. Trautmann, and A. Tucholski, Z. Phys. A **340**, 263 (1991).

[8] K. Hagel, M. Gonin, R. Wada, J. B. Natowitz, B. H. Sa, Y. Lou, M. Gui, D. Utley, G. Nebbia, D. Fabris, G. Prete, J. Ruiz, D. Drain, B. Chambon, B. Cheynis, D. Guinet, X. C. Hu, A. Demeyer, C. Pastor, A. Giorni, A. Lleres, P. Stassi, J. B. Viano, and P. Gonthier, Phys. Rev. Lett. **68**, 2141 (1992).

[9] H. Schulz, L. Muenchow, G. Roepke, and M. Schmidt, Phys. Lett B **119**, 12 (1982); H. Schulz, B. Kämpfer, H. W.

Barz, G. Roepke, and J. Bondorf, *ibid.* **147**, 17 (1984).
[10] P. J. Siemens, Nature **305**, 410 (1983).
[11] G. Bertsch and P. J. Siemens, Phys. Lett. **126B**, 9 (1983).
[12] H. R. Jaqaman, A. Z. Mekjian, and L. Zamick, Phys. Rev. C **27**, 2782 (1983); **29**, 2067 (1984).
[13] M. W. Curtin, H. Toki, and D. K. Scott, Phys. Lett. **123B**, 289 (1983).
[14] J. A. Lopez and P. J. Siemens, Nucl. Phys. **A431**, 728 (1984).
[15] A. D. Panagiotou, M. W. Curtin, H. Toki, D. K. Scott, and P. J. Siemens, Phys. Rev. Lett. **52**, 496 (1984); A. D. Panagiotou, M. W. Curtin, and D. K. Scott, Phys. Rev. C **31**, 55 (1985).
[16] L. P. Cernai and J. Kapusta, Phys. Rep. **131**, 223 (1986).
[17] J. Randrup and S. Koonin, Nucl. Phys. **A356**, 223 (1981); G. Gai and J. Randrup, *ibid.* **A381**, 557 (1982); Phys. Lett. **115B**, 281 (1982); Nucl. Phys. **A404**, 551 (1983).
[18] J. P. Bondorf, R. Donangelo, I. N. Mishustin, C. J. Pethick, H. Schulz, and K. Sneppen, Nucl. Phys. **A443**, 321 (1985); J. P. Bondorf, R. Donangelo, I. N. Mishustin, and H. Schulz, Nucl. Phys. **A444**, 460 (1985); H. W. Barz, J. P. Bondorf, P. Donangelo, I. N. Mishustin, and H. Schulz, *ibid.* **A448**, 753 (1986).
[19] D. H. E. Gross, X. Zhang, and S. Xu, Phys. Rev. Lett. **56**, 1544 (1986); X. Z. Zhang, D. H. E. Gross, S. Y. Xu, and Y. M. Zheng, Nucl. Phys. **A461**, 668 (1987); D. H. E. Gross, Rep. Prog. Phys. **53**, 605 (1990).
[20] L. G. Moretto, K. Tso, N. Colonna, and G. J. Wozniak, Phys. Rev. Lett. **69**, 1884 (1992).
[21] W. Bauer, G. F. Bertsch, and H. Schulz, Phys. Rev. Lett. **69**, 1888 (1992).
[22] L. G. Moretto, Phys. Lett. **40B**, 185 (1972); Nucl. Phys. **A247**, 211 (1975).
[23] A. Z. Mekjian, Phys. Rev. Lett. **38**, 640 (1977).
[24] W. A. Friedman and W. G. Lynch, Phys. Rev. C **28**, 16 (1983); **28**, 950 (1983).
[25] D. H. Boal, Phys. Rev. C **28**, 2568 (1983).
[26] C. R. Grant, Phys. Rev. C **34**, 1950 (1986).
[27] R. J. Charity, M. A. McMahan, G. J. Wozniak, R. J. McDonald, L. G. Moretto, D. G. Sarantities, L. G. Sobotka, G. Guarino, A. Pantaleo, L. Fiore, A. Gobbi, and K. Hildenbrand, Nucl. Phys. **A483**, 371 (1988).
[28] C. Barbagallo, J. Richert, and P. Wagner, Z. Phys. A **324**, 97 (1986); J. Richert and P. Wagner, Nucl. Phys. **A517**, 399 (1990).
[29] W. A. Friedman, Phys. Rev. Lett. **60**, 2125 (1988); Phys. Rev. C **42**, 667 (1990).
[30] D. J. Fields, W. G. Lynch, C. B. Chitwood, C. K. Gelbke, M. B. Tsang, H. Utsunomiya, and J. Aichelin, Phys. Rev. C **30**, 1912 (1984).
[31] D. J. Fields, W. G. Lynch, T. K. Nayak, M. B. Tsang, C. B. Chitwood, C. K. Gelbke, R. Morse, J. Wlczynski, T. C. Awes, R. L. Ferguson, F. Plasil, F. E. Obenshain, and G. R. Young, Phys. Rev. C **34**, 536 (1986).
[32] D. E. Fields, K. Kwiatkowski, D. Bonser, R. W. Viola, V. E. Viola, W. G. Lynch, J. Pochodzalla, M. B. Tsang, C. K. Gelbke, D. J. Fields, and S. Austin, Phys. Lett. B **220**, 356 (1989).
[33] D. R. Bowman, G. F. Peaslee, N. Colonna, R. J. Charity, M. A. McMahan, D. Delis, H. Han, K. Jing, G. J. Wozniak, L. G. Moretto, W. L. Kehoe, B. Libby, A. C. Mignerey, A. Moroni, S. Angius, I. Iori, A. Pantaleo, and G. Guarino, Nucl. Phys. **A523**, 386 (1991).
[34] J. L. Wile, D. E. Fields, K. Kwiatkowski, K. B. Morley, E. Renshaw, S. J. Yennello, V. E. Viola, N. Carlin, C. K. Gelbke, W. G. Gong, W. G. Lynch, R. T. de Souza, M. B. Tsang, and H. M. Xu, Phys. Lett. B **264**, 26 (1991).
[35] J. Aichelin, G. Peilert, A. Bohnet, A. Rosenhauer, H. Stocker, and W. Greiner, Phys. Rev. C **37**, 2451 (1988); G. Peilert, H. Stoecker, W. Greiner, A. Rosenhauer, A. Bohnet, and J. Aichelin, *ibid.* **39**, 1402 (1989).
[36] D. H. Boal and J. N. Glosli, Phys. Rev. C **38**, 1870 (1988); **38**, 2621 (1988).
[37] T. C. Sangster, H. C. Britt, D. J. Fields, L. F. Hansen, R. G. Lanier, M. N. Namboodiri, B. A. Remington, M. L. Webb, M. Begemann-Blaich, T. Blaich, M. M. Fowler, J. B. Wilhelmy, Y. D. Chan, A. Dacal, A. Harmon, J. Poulliot, R. G. Stokstad, S. Kaufman, F. Videbaek, Z. Fraenkel, G. Peilert, H. Stoecker, and W. Greiner, Lawrence Livermore National Laboratory Report No. UCRL-JC-108675, 1991.
[38] F. Zhu, W. G. Lynch, D. R. Bowman, R. T. de Souza, C. K. Gelbke, Y. D. Kim, L. Phair, M. B. Tsang, C. Williams, H. M. Xu, and J. Dinius, Phys. Lett. (to be published).
[39] W. Bauer, G. F. Bertsch, W. Cassing, and U. Mosel, Phys. Rev. C **34**, 2127 (1986); W. Bauer, Phys. Rev. Lett. **61**, 2534 (1988).
[40] K. Sneppin and L. Vinet, Nucl. Phys. **A480**, 342 (1988).
[41] H. W. Barz, J. P. Bondorf, R. Donangelo, H. Schulz, and K. Sneppin, Phys. Lett. B **228**, 453 (1989).
[42] M. Colonna, P. Roussel-Chomaz, N. Colonna, M. DiToro, L. G. Moretto, and G. J. Wozniak, Phys. Lett. B **283**, 180 (1992).
[43] R. T. de Souza, N. Carlin, Y. D. Kim, J. Ottarson, L. Phair, D. R. Bowman, C. K. Gelbke, W. G. Gong, W. G. Lynch, R. A. Pelak, T. Peterson, G. Poggi, M. B. Tsang, and H. M. Xu, Nucl. Instrum. Methods A **295**, 109 (1990).
[44] Y. D. Kim, R. T. de Souza, D. R. Bowman, N. Carlin, C. K. Gelbke, W. G. Gong, W. G. Lynch, L. Phair, M. B. Tsang, and F. Zhu, Phys. Rev. C **45**, 338 (1992).
[45] W. L. Kehoe, A. C. Mignerey, A. Moroni, I. Iori, G. F. Peaslee, N. Colonna, K. Hanold, D. R. Bowman, L. G. Moretto, M. A. McMahan, J. T. Walton, and G. J. Wozniak, Nucl. Instrum. Methods A **311**, 258 (1992).
[46] M. A. McMahan, G. J. Wozniak, C. M. Lyneis, D. R. Bowman, R. J. Charity, Z. H. Liu, L. G. Moretto, A. C. Mignerey, and M. N. Namboodiri, Nucl. Instrum. Methods A **253**, 1 (1986).
[47] C. Cavata, M. Demoulins, J. Gosset, M. C. Lemaire, D. L'Hote, J. Poitou, and O. Valette, Phys. Rev. C **42**, 1760 (1990).
[48] A. I. Warwick, H. H. Wieman, H. H. Gutbrod, M. R. Maier, J. Peter, H. G. Ritter, H. Stelzer, F. Weik, M. Freedman, D. J. Henderson, S. B. Kaufman, E. P. Steinberg, and B. D. Wilkins, Phys. Rev. C **27**, 1083 (1983).
[49] A. S. Hirsch, A. Bujak, J. E. Finn, L. J. Gutay, R. W. Minich, N. T. Porile, R. P. Scharenberg, B. C. Stringfellow, and F. Turkot, Phys. Rev. C **29**, 508 (1984); N. T. Porile, A. J. Bujak, D. D. Carmony, Y. H. Chung, L. J. Gutay, A. S. Hirsch, M. Mahi, G. L. Paderewski, T. C. Sangster, R. P. Scharenberg, and B. C. Stringfellow, *ibid.* **39**, 1914 (1989).
[50] S. J. Yennello, K. Kwiatkowski, D. E. Fields, R. Planeta, V. E. Viola, E. C. Pollacco, C. Volant, R. Dayras, R. Legrain, Y. Cassagnou, S. Harar, and E. Hourani, Phys. Lett. B **246**, 26 (1990); S. J. Yennello, E. C. Pollacco, K. Kwiatkowski, C. Volant, R. Dayras, Y. Cassagnou, R.

Legrain, E. Norbeck, V. E. Viola, J. L. Wile, and N. R. Yoder, Phys. Rev. Lett. **67**, 671 (1991).

[51] R. Lacey, N. N. Ajitanand, J. M. Alexander, D. M. de Castro Rizzo, P. DeYoung, M. Kaplan, L. Kowalski, G. La Rana, D. Logan, D. J. Moses, W. E. Parker, G. F. Peaslee, and L. C. Vaz, Phys. Lett. B **191**, 253 (1987); R. Lacey, N. N. Ajitanand, J. M. Alexander, D. M. de Castro Rizzo, G. F. Peaslee, L. C. Vaz, M. Kaplan, M. Kildir, G. La Rana, D. J. Moses, W. E. Parker, D. Logan, M. S. Zisman, P. DeYoung, and L. Kowalski, Phys. Rev. C **37**, 2561 (1988).

[52] I. M. Govil, J. R. Huizenga, W. U. Schroeder, and J. Toke, Phys. Lett. B **197**, 515 (1987).

[53] L. G. Moretto and D. R. Bowman, in Proceedings of the XXV International Winter Meeting on Nuclear Physics, Bormio, Italy, edited by I. Iori [Ricerca Scientifica ed Educazione Permanente, Suppl. 91 (1987)].

[54] L. G. Sobotka, M. A. McMahan, R. J. McDonald, C. Signarbieux, G. J. Wozniak, M. L. Padgett, J. H. Gu, Z. H. Liu, Z. Q. Yao, and L. G. Moretto, Phys. Rev. Lett. **53**, 2004 (1984); R. J. Charity, D. R. Bowman, Z. H. Liu, R. J. McDonald, M. A. McMahan, G. J. Wozniak, L. G. Moretto, S. Bradley, W. L. Kehoe, and A. C. Mignerey, Nucl. Phys. **A476**, 516 (1988); H. Y. Han, K. X. Jing, E. Plagnol, D. R. Bowman, R. J. Charity, L. Vinet, G. J. Wozniak, and L. G. Moretto, *ibid.* **A492**, 138 (1989); R. J. Charity, K. X. Jing, D. R. Bowman, M. A. McMahan, G. J. Wozniak, L. G. Moretto, N. Colonna, G. Guarino, A. Pantaleo, L. Fiore, A. Gobbi, and K. D. Hildenbrand, *ibid.* **A511**, 59 (1990).

[55] In the BUU calculations, the surfaces of the projectile and target are initially separated by 4 fm. For orientation, the velocity of an $E/A = 50$ MeV ^{129}Xe projectile is $0.32c$. At this velocity the time required to travel a distance equal to the sum of a ^{129}Xe radius plus a ^{197}Au radius is approximately 40 fm/c.

[56] $\langle \rho_{\rm res} \rangle$ also includes surface particles. Therefore $\langle \rho_{\rm res} \rangle$ has a value less than nuclear saturation density (≈ 0.16) even for a ground-state configuration. The initial decrease of $\langle \rho_{\rm res} \rangle$ at times < 10 fm/c is due to a relaxation following initialization. We have checked that this short relaxation time does not influence any results by starting the calculations with the projectile and target further apart.

[57] It should be noted that a single criterion of positive binding for each of the included test particle is not appropriate for determining the source properties. One can imagine very energetic test particles in the interior of the nucleus which are locally unbound, but which lose much of their energy through interactions with the mean field or other test particles before reaching the nuclear surface and, hence, remain bound. We have chosen to exclude only those unbound test particles near the nuclear surface which have little chance to interact further before they are emitted.

[58] The temperatures of the residues were calculated by assuming an ideal Fermi gas at the appropriate density and excitation energy per nucleon.